

All-mirror wavefront division interferometer for mid-infrared spectrometry

Ivan Zorin,^{1,*} Paul Gattinger,¹ Giovanna Ricchiuti,² Bernhard Lendl,² Bettina Heise,¹ and Markus Brandstetter¹

¹Research Center for Non-Destructive Testing, Science Park 2, Altenberger Str. 69, 4040 Linz, Austria

²Institute of Chemical Technologies and Analytics,
TU Wien, Getreidemarkt 9/164, 1060 Vienna, Austria

(Dated: May 29, 2024)

In this contribution, we address the core of any Fourier transform (FT) spectrometer—the interferometer—in perspective of the recent emergence of spatially coherent broadband infrared (IR) sources. As a result, we report on the design of a wavefront-division interferometer for spectroscopic applications in the mid-IR and beyond. The theoretical framework of the proposed wavefront division interferometer is discussed, and an analytical solution to determine the far-field interference pattern is derived. The solution is verified by both optical propagation simulations and experimentally. In view of the practical significance, we apply the wavefront division interferometer for FTIR spectroscopy. It features a simple architecture, ultra-broad achromaticity (limited only by the spectral profiles of the mirrors), high optical throughput, variable arms split ratio, and a two-fold increase in scan length and spectral resolution (demonstrated up to 0.2 cm^{-1}), respectively. Further, the employed design inherently enables the measurement of the complex refractive index. Experimental verification of the mentioned properties is provided by coupling the spectrometer with a mid-IR supercontinuum source for various applied spectroscopic studies: high-resolution transmission measurements of polymers (polypropylene) and gas (methane), as well as reflectance measurements of dried pharmaceuticals (insulin products on a metal surface).

I. INTRODUCTION

Fourier transform (FT) spectrometry is a mature and well-established technique that employs principles of low temporal coherence interferometry for high-resolution spectroscopic measurements[1, 2]. Its widespread adoption is attributed to the fundamental features of the FT spectrometer design, which has several distinctive and unique advantages over diffraction and dispersive systems[3]. The first advantage is the so-called multiplex sensitivity (Fellgett’s advantage. It is associated with simultaneous sampling of all spectral channels with a single detector that significantly boosts the signal-to-noise ratio, especially in infrared (IR) non-shot-noise limited systems. Another substantial sensitivity gain is linked to the optical étendue (Jacquinot’s advantage). In FT spectrometry, the spectral resolution is unconditional on the geometric and optical parameters of the system, such as grating period and slit size. It thus depends solely on the scan length as a reciprocal. Consequently, there’s no requirement for spatial filtering using input slits or apertures. As a result, FT spectrometers feature high spectral resolution with large optical apertures and, thus, throughput. Furthermore, a standard FT system is backed by a reference laser to linearize the signals while scanning the interferometer arm, leading to a third advantage: prior knowledge of the reference laser’s wavelength ensures the high accuracy of time domain measurements and subsequent Fourier domain reconstruction. The spectral response of state-of-the-art IR FT spectrometers is broad and normally limited by the

detector responsivity and spectral properties of transmission components used in the particular design. Driven by interests of IR spectroscopy, most commercial instruments operate in the near- and mid-IR ranges but require either the replacement of a detector or optics to switch between the spectral windows. Technical advantages, affordability, as well as relative simplicity have made FTIR spectroscopic techniques a standard routine tool for chemical analysis in research[4–6], as well as in biomedical[7–10], and industrial applications[11–14].

The main components of any FT spectrometer are a light source, a detector, and an optical interferometer. The interferometer’s role is to perform the autocorrelation of the source’s electric field, enabling the sequential reconstruction of amplitude or phase spectra according to the Wiener-Khinchin theorem. Concerning the optical scheme, in most scenarios, even for advanced on-chip realizations[15, 16], a Michelson-type arrangement with a single amplitude divider (such as a plate beam splitter) is used[17, 18]. The core interferometer can be, however, advanced mechanically, or its optical part can be extended to other measurement modalities, such as attenuated total reflection, imaging or mapping, using additional components or optics[19]. Thus, the range of different implementations of FTIR spectroscopic techniques is fairly wide[2].

In terms of emitters, conventional scanning FT spectrometry offers versatility by accommodating a wide range of broadband light sources without requiring specialized properties. This primarily includes extended blackbody emitters, which represent the state-of-the-art solution. Nevertheless, owing to the rapid development of mid-IR photonics, many ultra-bright broadband spatially coherent laser sources have been developed in the last decades, greatly enriching the IR spectroscopy field.

* ivan.zorin@recendt.at

Such laser sources are uni-directional, high-power, and provide brightness that is orders of magnitude higher than that of thermal sources[20, 21]. Since the product of brightness and étendue is the spectral power that the optical system transmits and employs to probe the sample, mid-IR lasers represent a promising alternative for IR spectroscopy. Among the broad variety of options, supercontinuum sources, characterized by an intrinsic bright and instantaneous ultra-broad emission, are particularly well-suited for FT interferometric methods. Supercontinuum generators are nonlinear laser-driven emitters that feature high laser-like spatial but low temporal coherence (due to the ultra-broad emission profiles)[22], a desired combination for the FT techniques. Recent advances in supercontinuum sources confirm this and provide illustrative evidence of their advantages in spectroscopy[23]. In particular, recent reports of ultra-broad (covering functional and fingerprint regions and ranges inaccessible to quantum cascade lasers) high-intensity realizations are particularly prospective[24, 25]. Nevertheless, due to the particular properties of supercontinua, the techniques have to be often adapted.

Various aspects of adapting instruments for use with supercontinuum sources have been addressed in recent years. Concerning signal acquisition, for instance, the importance of using demodulation techniques to increase the signal-to-noise ratio has been discussed[26, 27]. Besides, more advanced schemes combining demodulation and balanced detection to eliminate intensity noise have been proposed[28, 29]. In this contribution, we target to re-examine the basis of any FT spectrometer—the interferometer—in light of the recent development of ultra-broadband spatially coherent sources. Thus, we propose an alternative optical design of an all-mirror wavefront division interferometer. In the first part, we present a theoretical framework describing interferometric signals, which we relate to experimental data and optical propagation simulations. In the experimental part, the performance of the interferometer is evaluated for FTIR spectroscopy. The developed optical system has no transmission optics and is thus broadly achromatic, with the potential to operate from the ultraviolet to terahertz range. In our design, we exploit the high spatial coherence of the light source to perform lossless division and recombination of the beams. The wavefront division scheme provides a significant improvement over the losses typical for conventional amplitude-division beam splitters. In addition, the selected division method allows the splitting ratio to be freely adjustable, enabling precise dynamic range adjustment in case of low- or high-absorbing samples. Another characteristic feature of the design is a 2-fold (potentially 4-fold) increase in scan length, which yields high spectral resolution. Finally, we demonstrate spectroscopic measurements of various practically interesting samples. Since the system is inherently capable of measuring the complex refractive index, such measurements are also presented. The spectrometer’s performance is demonstrated for routine spectroscopic mea-

surements using a state-of-the-art mid-IR supercontinuum laser.

II. WAVEFRONT DIVISION INTERFEROMETER: THEORY AND SIMULATIONS

The basic linearized optical scheme of a wavefront division interferometer is shown in Fig. 1 (experimental implementation in the FT spectrometer modality—is displayed in Fig. 6 of the next section). The input beam of the high spatial coherence source $g(S_x)$ is divided into two parts $E_L(S_x)$ and $E_R(S_x)$, forming two interferometer arms, respectively. A phase difference ($\Delta\phi$) can be introduced independently for a single arm. The two previously divided beams combine again into a single beam (resembling the input one) on a combining optical element. The recombined beams produce an interference pattern in the far field of the system, enabling the analysis of the phase and amplitudes of the waves. It has to be noted that the split ratio between the arms can be broadly adjusted by translation of the divider in the lateral dimension across the input beam.

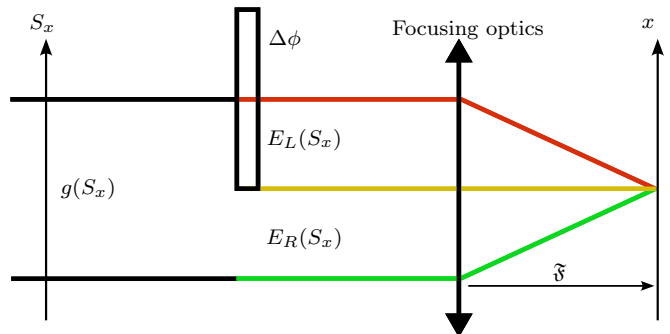


FIG. 1: Linear scheme of the wavefront division interferometer, simplified: the input beam ($g(S_x)$) is wavefront-divided into two parts ($E_L(S_x)$ and $E_R(S_x)$) by a binary rectangular aperture, whereby the phase delay is introduced for the parts independently; the sub-beams combined again into one single beam are focused, creating an interference pattern in the far field.

The proposed interferometer, akin to the most well-known Young wavefront division interferometer, exhibits a spatial interference pattern in the lateral dimension. This distinguishes it from the axial modulation (for flat wavefronts) in Michelson amplitude division interferometry. Since the beam after recombination is similar to the input beam with negligible diffraction artifacts, interference is only observed in the focal plane where the paths are indistinguishable[30].

The interference pattern can be accessed by optical propagation simulations—in our case performed using a free Python toolkit[31]—and in analytical form. For simplicity, we consider the analytical form just for one dimension where the wavefront division takes place; the S_x

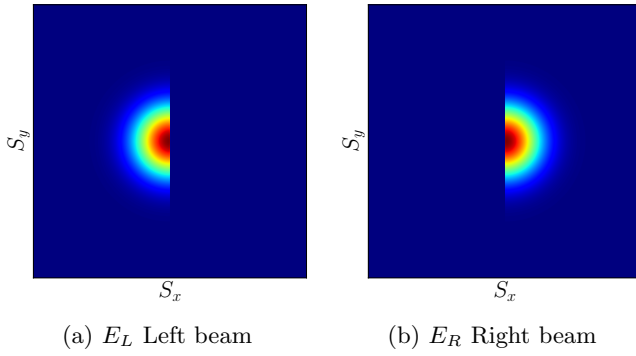


FIG. 2: Beam intensity profiles of the interferometer arms after wavefront division; taken at distance 0 (no diffraction).

and x coordinates are of relevance for modeling. The input field can be modeled with a Gaussian intensity profile (a valid approximation for spatially coherent laser sources) and constant phase ϕ as:

$$g(S_x) = e^{-S_x^2} e^{i\phi}, \quad (1)$$

where S_x is the spatial coordinate in the near-field division plane (further S_y is orthogonal to S_x).

In the case of a 50/50 split ratio, to which we limit our analytical representation, the act of wavefront division can be expressed as a product of the input field with the Heaviside step function:

$$E_L(S_x) = g(S_x)H_L(S_x), \quad (2)$$

where $H_L(S_x)$ is the Heaviside step function for the one-half of the beam (L indicates "left" for simplicity), defined as:

$$H_L(S_x) = \begin{cases} 1 & S_x < 0 \\ 0 & S_x \geq 0 \end{cases}. \quad (3)$$

The Heaviside step function for the second arm (right R) is then represented as:

$$H_R(S_x) = \begin{cases} 0 & S_x < 0 \\ 1 & S_x \geq 0 \end{cases}, \quad (4)$$

with the field defined as:

$$E_R(S_x) = g(S_x)H_R(S_x). \quad (5)$$

The resulting beams are shown in Fig. 2 for illustrative purposes; the beam after recombination showing near-field diffraction is shown in Fig. 3.

Accessing the interference pattern formed in the focus plane (exemplified for a paraxial positive lens in Fig. 1) involves employing a Fraunhofer diffraction equation, which can be reduced to a Fourier transform in the far field[32]. According to the convolution theorem, the

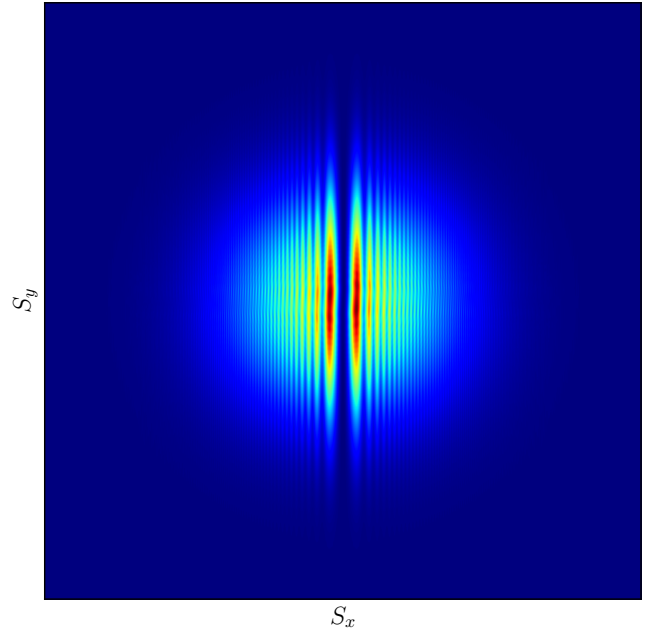


FIG. 3: Intensity profile of the recombined beam; near-field diffraction is observed.

Fourier transform of the product of two functions equals the convolution of the Fourier transforms of those functions. Therefore, in the far field, each of the interfering fields can be represented as a convolution of their corresponding Fourier representations:

$$E_R(x) = \mathfrak{F}\{g(S_x)\} * \mathfrak{F}\{H_R(S_x)\}, \quad (6)$$

$$E_L(x) = \mathfrak{F}\{g(S_x)\} * \mathfrak{F}\{H_L(S_x)\}, \quad (7)$$

where x is the spatial coordinate in the far field. The Fourier representations of Gaussian functions preserve the Gaussian shape:

$$\mathfrak{F}\{g(S_x)\} = \sqrt{\pi} e^{-x^2} e^{-i\phi}, \quad (8)$$

for simplicity, we omit the $1/4$ factor in the exponent of the Fourier transform of the Gaussian function.

The Fourier transform of the Heaviside function is given by [33]:

$$\mathfrak{F}\{H_{L/R}(S_x)\} = \frac{1}{2} \left\{ \delta(x) \pm \frac{i}{\pi x} \right\}, \quad (9)$$

where $\delta(x)$ is the Dirac delta function, and the sign depends on whether the step is left- or right-sided. Thus the convolutions defined in Eqs. 6 and 7 take the form of:

$$E_{R/L}(x) = \frac{1}{2} \text{p.v.} \int_{-\infty}^{\infty} \mathfrak{F}\{g(S_x)\} \left[\delta(x - x') \pm \frac{i}{\pi(x - x')} \right] dx'. \quad (10)$$

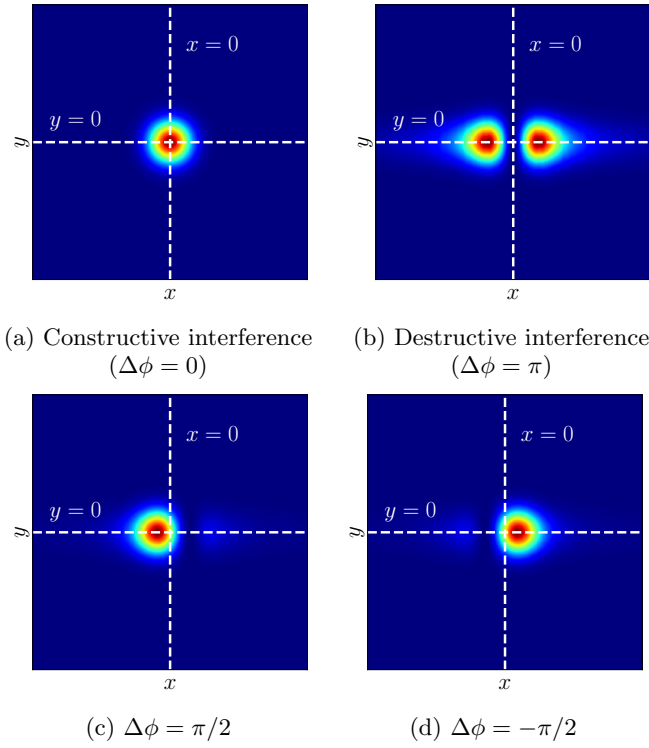


FIG. 4: Lateral interference patterns in the far field of a wavefront division interferometer for different representative values of phase delays.

The first term in the convolution is the convolution of the Gaussian function with the delta function, so it remains unchanged, and the second term is in the form of a Hilbert transform. Using the following Hilbert transform pair[34]:

$$f(x) = e^{-x^2} \rightarrow H(f(x)) = -e^{-x^2} \operatorname{erfi}(x), \quad (11)$$

where $\operatorname{erfi}(x)$ is the imaginary error function, it is possible to derive the fields as follows:

$$E_R(x) = \frac{\sqrt{\pi}}{2} \left[e^{-x^2} e^{-i\phi_R} - i e^{-x^2} e^{-i\phi_R} \operatorname{erfi}(x) \right], \quad (12)$$

and for the second half as:

$$E_L(x) = \frac{\sqrt{\pi}}{2} \left[e^{-x^2} e^{-i\phi_L} + i e^{-x^2} e^{-i\phi_L} \operatorname{erfi}(x) \right], \quad (13)$$

respectively. The phases ϕ_L and ϕ_R of the fields are decoupled and can be changed independently. Thus, the interference pattern in the focal plane can be derived as a coherent sum of incident fields:

$$I(x) = \langle (E_R(x) + E_L(x))(E_R(x) + E_L(x))^* \rangle. \quad (14)$$

Substituting Eqs. 12 and 13, Eq. 14, after meticulous calculations takes the following elegant form:

$$I(x) = \pi e^{-2x^2} \left[\cos \frac{\Delta\phi}{2} + \operatorname{erfi}(x) \sin \frac{\Delta\phi}{2} \right]^2, \quad (15)$$

where $\Delta\phi = \phi_R - \phi_L$. It should be noted that the outcome obtained in Eq. 15 interestingly resembles the form of a fractional Hilbert transform[34, 35].

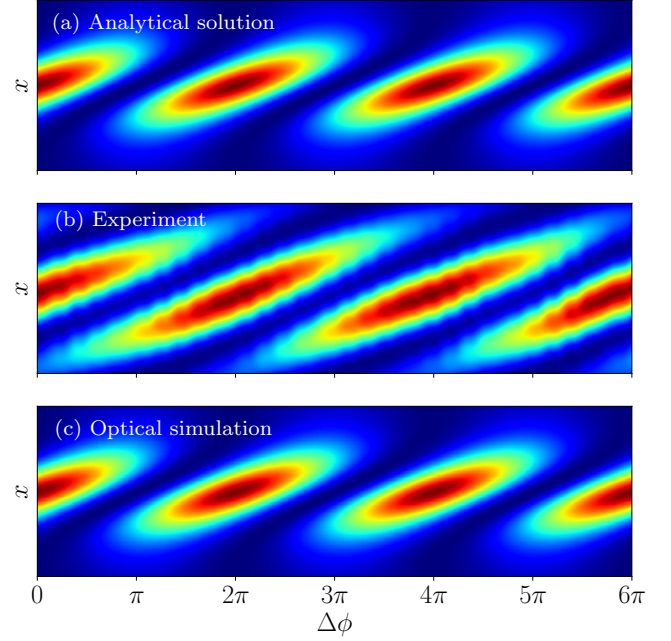


FIG. 5: Far-field interference patterns in the wavefront division interferometer: (a) analytical solution, (b) experimental data, and (c) optical simulations; displayed in for $y = 0$ (wavefront division plane, centered for x), the plane corresponds to the $y = 0$ white dashed line in Fig. 4; for the experimental data, the x-axis has a size of $550 \mu\text{m}$ (100 px), the pixelated structure is due to the limited temporal resolution of the camera during fast phase scanning.

Equation 15 describes the far-field lateral intensity profile and provides a clear indication of the overall asymmetric behaviour of the interference pattern in the wavefront division interferometer of the proposed type. Thus, in the case of constructive interference (i.e., $\Delta\phi = 0$), the term containing the imaginary error function turns zero, resulting in a centered Gaussian maximum. In the case of destructive interference (i.e., $\Delta\phi = \pi$), the pattern shows a minimum at the center, on the optical axis ($x = 0$, $y = 0$), with two pronounced peaks around it. Asymmetric behavior can also be observed in the case of $\Delta\phi = \pi/2$ and $\Delta\phi = -\pi/2$, as the change of sign constructively intensifies one side and suppresses the other. These cases are summarized in Fig. 4; we omit the scales for x and y axes as they are not of practical importance. It should be noted that the generalized solution for non-50/50 split ratios is quite bulky, as it would contain more terms in the sum defined in Eq. 14. For non-centered Heaviside functions, the shift in the near-field domain implies additional spatial components in the Fourier domain, so the pattern will retain asymmetry. For this reason, we consider only a special case and propose to

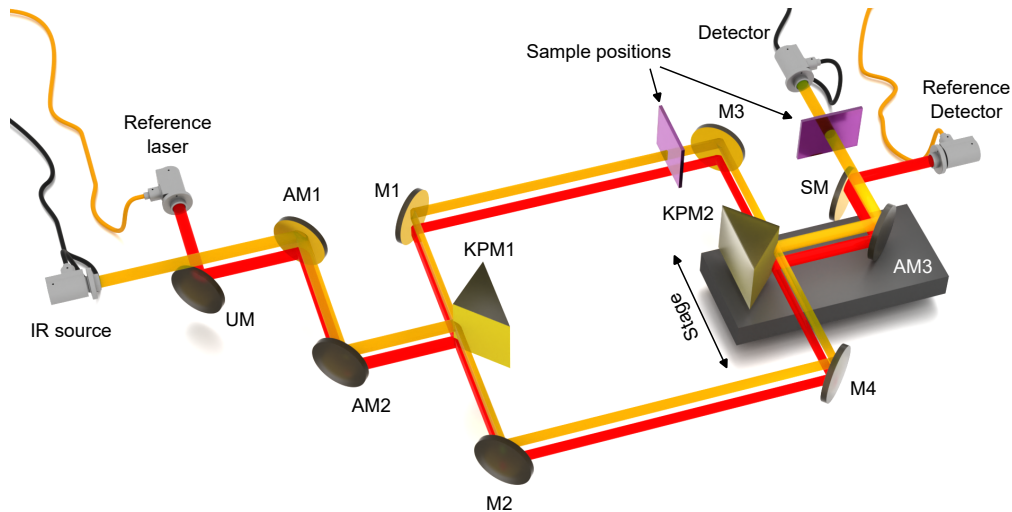


FIG. 6: Fourier transform IR spectrometer based on an all-mirror wavefront division interferometer: UM and SM are uniting and separating mirrors respectively coupling two sources to the interferometer at different heights; AM- alignment mirrors; KPM1 and KPM2 are knife-edge prism mirrors dividing and recombining the input wavefront; M1-M4 are flat mirrors of the interferometer arms that form the interferometer together with the KPMs. KPM2 is mounted on a linear stage to vary the length of both arms in time; two possible sample positions are indicated.

use optical simulations for complex split ratios.

In order to verify the analytical solution and the results obtained with optical propagation simulations, we evaluated the far-field interference patterns experimentally. For this purpose, the optical arrangement of the wavefront division interferometer, discussed in detail in Section III, was used. A quasi-monochromatic helium-neon laser (632.8 nm) was used to obtain a clear interference pattern. After beam recombination, the far-field image was acquired using a lens with a focal length of 400 mm. The long focal length was used to ensure that the camera (Ximea, xiQ, MQ022RG-CM, 5.5 μm pixel size, operated at 700 fps) had enough pixels to resolve the image. The phase ϕ has been scanned using a linear translational stage.

The experimental data, matched with the results of the simulations[31] and the analytical solution (obtained using Eq. 15), are shown in Fig. 5. The results are displayed for the $x\Delta\phi$ plane (spatial coordinate in the middle of the beam [$y = 0$] and phase delay). The findings are in good agreement. The overall asymmetric behaviour is well distinguished. The slight deviation between the experimental and computed data can be attributed to astigmatism, different initial beam profile and, for example, camera positioning not exactly in the focus.

The results obtained in this section establish the theoretical basis for the interferometer design. The gained outcomes also have practical significance. For example, for point detector measurements, it can be seen that the size of the detector should be smaller than the size of the entire interference pattern. Otherwise, integration over the xy plane will nullify the modulation depth.

III. WAVEFRONT DIVISION FOURIER TRANSFORM IR SPECTROMETER

The practical implementation of an all-mirror FT spectrometer based on the introduced principles of wavefront division interferometry is shown in Fig. 6. As in a conventional amplitude division FT spectrometer, the system employs two light sources: a broadband IR source (mid-IR supercontinuum source with high spatial coherence) and a quasi-monochromatic reference laser (continuous wave helium-neon laser). The employed supercontinuum source (NKT Photonics, SuperK, $\text{ZrF}_4\text{-BaF}_2\text{-LaF}_3\text{-AlF}_3\text{-NaF}$ fiber based) provides a broadband emission coverage in the range from 1.1 μm to 4.4 μm (the near-IR part containing a strong pump line at 1.55 μm is excluded using a spectral filter). The system operates at a 2.5 MHz repetition rate; the average power is about 490 mW. The beam quality M^2 is 1.09. The reference laser is deployed to produce a distinct high-quality sinusoidal interferogram, which is utilized to linearize the low-coherence IR interferogram during the mechanical scanning of the arms. The beams are co-aligned to enter the interferometer at different heights using a uniting mirror (UM), i.e. they are collinear along the optical axis. The size of the optical components allows them to be handled separately.

The beams are guided normally to the first knife-edge right-angle gold prism (KPM1), which divides the wavefront and thus forms the arms of the interferometer. The two halves of the input fields (assuming a 50/50 split ratio) are directed by the interferometer mirrors (M1-M4) to another identical prism, KPM2, where the combination takes place. Hence, the interferometer resem-

bles a Mach-Zehnder type configuration with a symmetric right-angle arrangement formed by four mirrors. The IR and reference beams are separated the same way they were combined by a separating mirror (SM). The interference pattern is recorded in the far field using corresponding single-point detectors. In the experimental setup, the light is coupled into single-mode optical fibers to facilitate connection to the detector and, e.g., to a reflection measurements head (in case of reflection measurements). Off-axis parabolic mirror couplers are used so that the far-field image is formed directly in the plane of the fiber cores. A small longitudinal translation of KPM2 (perpendicular to the path length scanning) enables—akin to induced astigmatism—scaling of the interference pattern in the focal plane to achieve high interference visibility (integrating over the core area). This is a direct consequence of the theoretical considerations discussed in the previous section. A simple pinhole with properly selected optics (to not sacrifice the throughput) or a single-point detector with long-focus mirrors can be used for the same purpose. In the developed spectrometer, the mirror was aligned using a manual stage to maximize interference visibility.

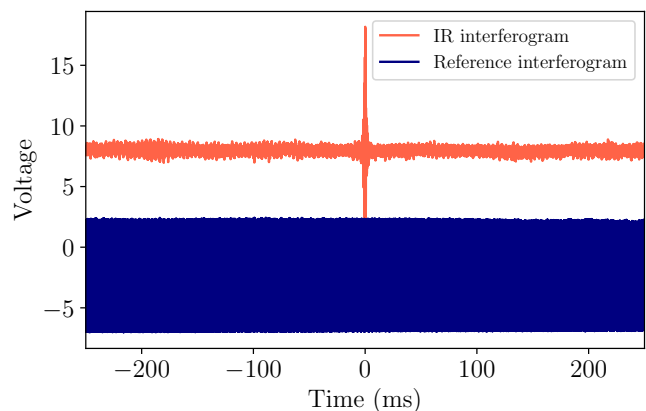
In order to emphasize the broadband nature of the designed spectrometer, a novel fast mid-IR pyroelectric detector (Laser Components, PR No.1) capable of operation from UV to THz range has been employed. The IR detector has an ultra-thin LiTaO_3 pyroelectric layer (6 μm) thus providing a high responsivity of 70000 V/W (typical) and a detectivity of $2 \times 10^8 \text{ cm} \cdot \sqrt{\text{Hz}}/\text{W}$ (at 1 kHz). The bandwidth of the detector is extended up to 100 kHz[36]. Since pyroelectrics are sensitive to alternative signals, i.e., temperature changes, the system is well suited to the principles of FT spectrometry. The modulation induced by interference (time-varying component) is detected directly. Thus, the IR interferograms are captured and mean-centered at zero, with the constant component excluded inherently. Since the detector is slower than photonic detectors, the pulses of the source are naturally integrated, and no demodulation is required. It should be noted that despite the high sensitivity, the pyroelectric detector has a limited dynamic range. In order to avoid oversaturation, the light intensity is controlled in front of the sensitive area. The reference interferograms were recorded using a visible photo-receiver (Femto HCA-S).

Arm length differences are scanned by lateral scanning of the KPM2 using a motorized linear stage (Zaber, X-LHM050A-E03). It should be noted that the KPM2 scanning simultaneously varies the length of both arms, effectively doubling the scanning range. An alignment mirror AM3 is fixed on the same stage to ensure pointing stability after the interferometer.

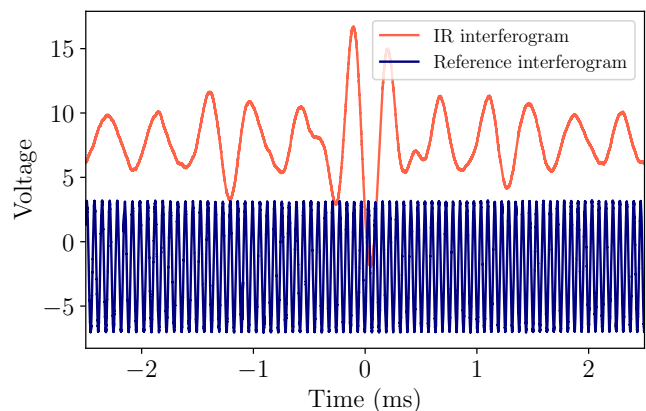
There are two possible sample locations in the system. For IR transmission measurements, the sample can be placed either in the combined beam or in one of the interferometer's arms. The first case resembles the standard scenario of absorption measurements in conventional sys-

tems. The latter case is of particular interest because the wavelength-specific phase delay (dispersion) introduced by the sample remains uncompensated and hence enables complex refractive index measurements. IR dispersion spectroscopy is of major applied relevance due to the linear dependence of the refractive index on the concentration—beyond the validity of the Bouguer–Beer–Lambert law[37, 38]. On the other hand, positioning the sample in the combined beam is reasonable, for example, for reflectance or attenuated total reflection measurements, since no change in the interferometric arm scheme is required.

The signals in the developed FT spectrometer were recorded using an oscilloscope (Teledyne Lecroy, HDO6104A, 1 GHz bandwidth, 10 GS/s). One channel is allocated to the IR interferogram and the other to the reference interferogram. The post-processing of the



(a) Raw interferograms: 500 ms base (10 mm/s speed)



(b) Raw interferograms: zoomed-in, 5 ms base

FIG. 7: Typical raw interferograms captured using the developed Fourier transform spectrometer: a low-coherence IR interferogram (obtained for the broadband IR supercontinuum source) and the reference signal (obtained for the quasi-monochromatic helium-neon laser).

recorded interferograms was implemented in the Python environment. The developed algorithm involved kernel linearization, apodization (Blackman–Harris window), zero padding, and Fourier transform.

Figure 7 displays raw unprocessed wavefront division interferograms (the reference signal is offset by 7.5 V for clarity) recorded with the oscilloscope.

IV. RESULTS

In this section, IR spectroscopic measurements performed with the developed FT spectrometer are presented. The capabilities of the system are demonstrated in several applied scenarios. As it has been discussed previously, the system is capable of high-resolution measurements owing to the doubled scan length. Thus, prior to demonstrating the spectroscopic measurements, in Fig. 8 we display the power spectral density of the used supercontinuum source recorded with the developed FT spectrometer. The total scan length for this measurement is 5 cm, so the achieved spectral resolution is 0.2 cm^{-1} , which is relatively high compared to state-of-the-art commercial systems.

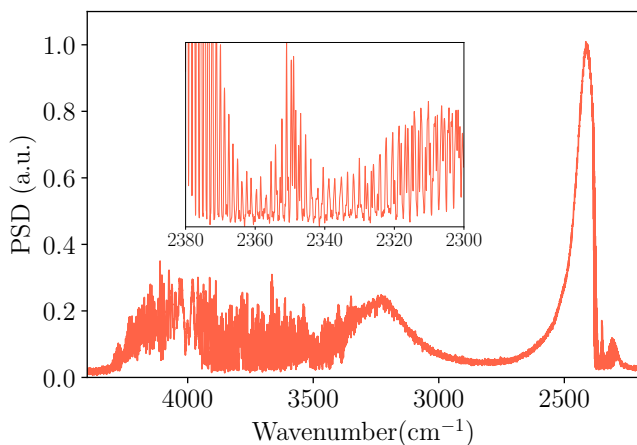


FIG. 8: Normalized emission power spectral density of the IR supercontinuum source measured using the developed wavefront division spectrometer at a spectral resolution of 0.2 cm^{-1} ; due to the high resolution, the sharp absorption of ambient water vapour is observed, the inset depicts the magnified absorption band structure of ambient CO_2 .

The measurements presented in this section are performed at different spectral resolutions but at the fixed stage scan speed of 12 mm/s (effectively doubled to 24 mm/s). Thus, for instance, for 0.4 cm^{-1} spectral resolution, a single measurement takes around 1 sec.

A. Transmission measurements: gas

In order to demonstrate the capability of the developed spectrometer for high-resolution detection and analysis of gases, transmission measurements of methane (CH_4) were performed. The absorption measurements were carried out in the combined beam configuration. As a sample, a 10 cm long sealed gas cell (Wavelength References) with 100 Torr CH_4 (balanced with N_2 to 500 Torr) was used. Methane exhibits strong and fine spectral features

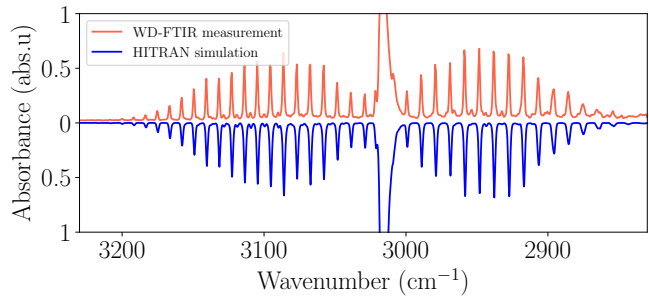


FIG. 9: Absorbance spectra of methane measured with the developed Fourier transform wavefront division spectrometer (WD-FTIR), the blue line shows a HITRAN database simulation (for reference).

in the mid-IR range at around 3019 cm^{-1} attributed to vibrations of C-H (fundamental triply degenerate asymmetric stretching)[39]. Since methane is a greenhouse gas, as well as an important combustion-related species, the measurements also emphasize practical potential.

Figure 9 depicts an absorbance spectrum calculated according to the Bouguer–Beer–Lambert law (decadic form) as:

$$A(\tilde{\nu}) = -\log_{10} \left[\frac{I(\tilde{\nu})}{I_0(\tilde{\nu})} \right], \quad (16)$$

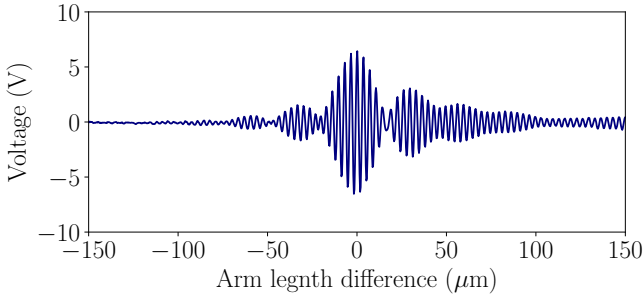
where I and I_0 are the intensities of transmitted and incident radiation, respectively, and $\tilde{\nu}$ is the wavenumber. The measurement is performed at around 1.4 cm^{-1} resolution. A higher resolution is feasible (as demonstrated before) but impractical. The spectral lines are subject to collision broadening because the gas is under relatively high pressure. In addition, the absorption in this range is quite strong, which leads to full absorption at high resolution.

Figure 9 also displays an absorbance spectrum simulated using the HITRAN spectroscopic database[40] for the exact given cell parameters. It should also be noted that the absorption in the Q branch is strong, leading to total absorption. For this reason, the plots are constrained and focus primarily on the P and R branches.

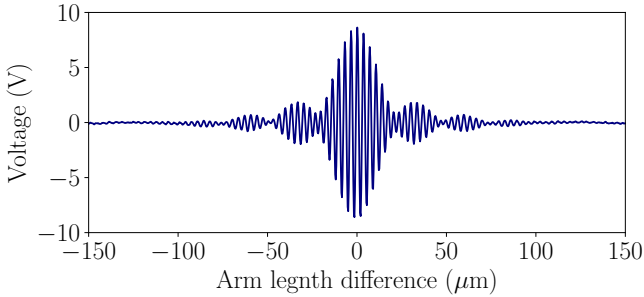
B. Complex refractive index measurements: polypropylene

In this subsection, measurements of the complex refractive index for a solid sample, a thin polymer film, are demonstrated and exemplified. As a sample, a 6 μm thick polypropylene film was used (Chemplex Industries, inc., Cat.No.425).

The sample has been placed in one arm of the interferometer, thus, in addition to absorption, causing uncompensated group velocity dispersion, i.e., different frequencies propagate with nonlinearly related phase velocities. Therefore, the IR interferograms appear broadened and asymmetric. Such a raw interferogram for a polypropylene film and a reference interferogram (no sample inserted) are shown in Figs. 10a and 10b respectively.



(a) IR interferogram with a polypropylene film inserted



(b) Dispersion-free IR interferogram (sample not inserted)

FIG. 10: IR interferograms for the reference measurement (dispersion-free, no sample insertion) and the complex refractive index measurement (the polypropylene film is in one of the arms of the interferometer).

The result of the Fourier transform in the general case has a complex form. In absorption measurements, only real-valued magnitude spectra are evaluated. However, the phase spectra representing the frequency-specific delay can be utilized to access the uncompensated dispersion, i.e., the sample is in one of the arms only. More details on the calculation procedure in dispersive or so-called asymmetric FT spectroscopy can be found in the specialized literature[2, 37, 41–43].

The phase is derived from the imaginary and real parts

of the Fourier transform spectrum as:

$$\phi(\tilde{\nu}) = \arctan \left[\frac{\text{Im}\langle \mathfrak{F}(S(\delta)) \rangle}{\text{Re}\langle \mathfrak{F}(S(\delta)) \rangle} \right], \quad (17)$$

where $S(\delta)$ represents the raw signal that depends on the arm length difference δ . In order to obtain smooth phase spectra, the calculated phase (Eq. 17) is unwrapped using phase unwrapping algorithms (Python-based algorithms were employed). The reference phase spectrum (corresponds to a linear slope as it induces a shift) is then subtracted from the sample phase spectrum, resulting in a net sample-induced phase difference $\Delta\phi$. Since the thickness of the sample d is known, the refractive index variations can be obtained in the following form:

$$\Delta n(\tilde{\nu}) = -\frac{\Delta\phi(\tilde{\nu})}{2\pi d\tilde{\nu}}. \quad (18)$$

The dispersion profile of the sample is shown in Fig. 11.

Polypropylene features an absorption band within the

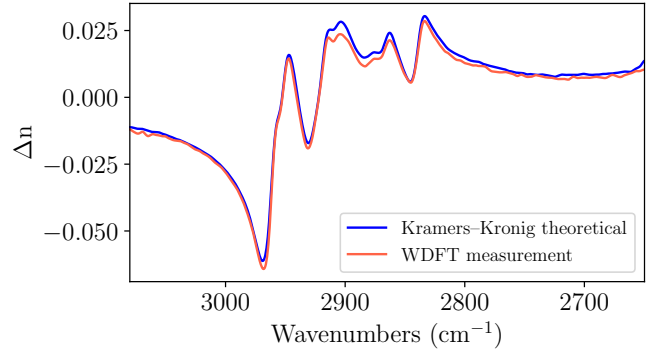


FIG. 11: Dispersion spectrum of polypropylene (anomalous, near an absorption band) measured and compared to the theory (derived using the Kramers-Kronig dispersion relation).

emission window of the source. The absorption has a distinct shape and is caused by symmetric and asymmetric stretching vibrations of CH_3 and CH_2 functional groups[44]. Therefore, a particularly interesting region of an anomalous dispersion can be observed and evaluated as depicted in Fig. 11.

The direct dispersive spectroscopy measurements depicted in Fig. 11 are verified using the bidirectional Kramers–Kronig relations that connect the real and imaginary parts of the complex refractive index. For the real part of the refractive index, the relation is defined as:

$$\Delta n = \frac{1}{\pi} \text{p.v.} \int \frac{\tilde{\nu}' k(\tilde{\nu}')}{\tilde{\nu}'^2 - \tilde{\nu}^2} d\tilde{\nu}', \quad (19)$$

where $k(\tilde{\nu})$ is the extinction coefficient (imaginary part of the refractive index). Since spectroscopic transmittance measurements yield both the absorption and dispersion

properties of the sample, the extinction coefficient can be directly obtained from the absorption coefficient $\alpha(\tilde{\nu})$ as:

$$k(\tilde{\nu}) = \frac{\alpha(\tilde{\nu})}{4\pi\tilde{\nu}}, \quad (20)$$

where the absorption coefficient can be calculated using the Bouguer-Beer-Lambert law (exponential form), since:

$$-\ln \frac{I(\tilde{\nu})}{I_0(\tilde{\nu})} = \alpha(\tilde{\nu})d. \quad (21)$$

Hence, the direct measurement is in remarkably good agreement with the theoretical profile (highlighted in blue in Fig. 11). The calculated extinction coefficient is shown in Fig. 12. The high quality of the absorp-

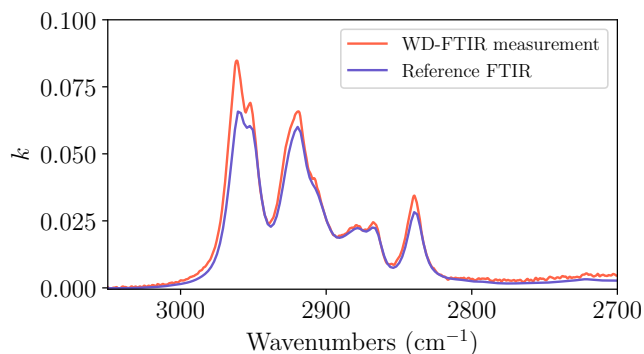


FIG. 12: Extinction coefficient (imaginary part of the refractive index) of polypropylene measured with the developed FT wavefront division spectrometer; the measurement obtained with a conventional state-of-the-art FTIR spectrometer is shown for comparison.

tion measurement is confirmed by a reference measurement obtained with a standard state-of-the-art commercial FTIR spectrometer (Bruker, Vertex 70, see Fig. 12).

C. Reflection measurements: insulin products

In this section, we demonstrate another measurement mode: reflection measurements. The proposed FT scheme relies on the high spatial coherence of light sources, thus offering inherent advantages for this measurement modality. As the properties are related, sources with high spatial coherence typically exhibit an M^2 value close to 1 and excellent spectral brightness. This characteristic enables the removal of the common trade-off between spatial resolution and sensitivity found in state-of-the-art FTIR- and micro-spectrometry and based on thermal emitters[45]. Consequently, the same measurements can be accomplished using wavefront division interferometry but with a higher speed and signal-to-noise ratio. Spatial resolution, which depends on the beam quality and optics, can approach or reach the diffraction

limit. These factors indicate the high potential of the developed approach for various hyperspectral imaging applications, in particular for chemical mapping. Here, as a proof of concept, we demonstrate a single-point measurement without spatial scanning.

The reflection measurements were realized in the combined beam scenario. Modifications in one arm of the interferometer necessitate matching the arm length of the other arm. Therefore, the manipulation of the combined beam is more feasible in the case of the reflection geometry. The combined beam was coupled into a single-mode fluoride fiber and connected to a reflection measurements head, where it was collimated using a reflective off-axis parabolic mirror. The high-quality fundamental Gaussian beam of around 12 mm $1/e^2$ diameter was then focused onto the sample using a low-NA ZnSe lens (200 mm). The spot size in the focus is estimated to be around 70 μm . The reflection geometry implied a small angle between the incident and reflected beams, facilitating path separation and eliminating the need for beam splitters. The reflected light was then collected and focused onto the detector using an off-axis parabolic mirror.

The sample selected for analysis was a dried commercial insulin product deposited on a stainless steel substrate. This choice is particularly relevant as it represents a typical scenario in the pharmaceutical industry, where equipment surfaces must be cleaned between production runs to minimize contamination risks. Therefore, precise control is essential to reduce cleaning cycles, making the demonstrated application of practical value. The sample was quantified to contain approximately 130 $\mu\text{g}/\text{cm}^2$ of the insulin drug product (average value affected by a coffee-stain effect) that comprised: active pharmaceutical ingredient (insulin, main component), glycerol (main excipient), and in smaller concentrations M-cresol, phenol, and sodium phosphate dibasic dihydrate.

The relevant part of the absorbance spectrum of the compounded insulin formulation, measured in reflection, is displayed in Fig. 13. For this chemically complex

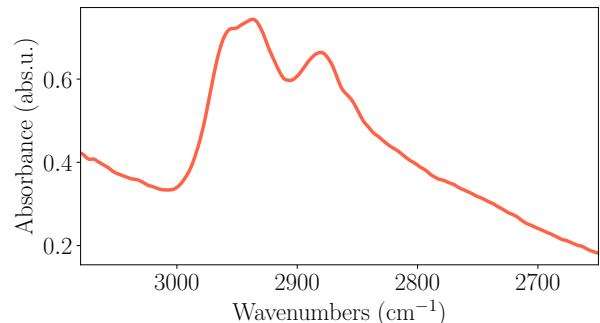


FIG. 13: Absorbance spectrum of the dried insulin product deposited on a stainless steel substrate measured in reflection geometry (the spot size is around 70 μm).

sample (combining the weighted absorbance of comprising compounds), a very good agreement with publicly available scientific reports was found. An extensive and specialized review containing measurements and detailed discussions of the IR spectra of insulin products was performed by Sven Delbeck and Herbert Michael Heise[46]. The shape of the absorbance profile closely matches the reported ones, and the pronounced spectral features are preserved.

V. DISCUSSION AND CONCLUSION

We have presented a scheme of a wavefront division interferometer relying on sources with high spatial coherence. The system can potentially operate from the ultraviolet to terahertz range. The theoretical framework governing the interference pattern has been provided and verified through optical propagation simulations and experimentally. Regarding the general operational principles of the proposed wavefront division system, an extensive literature review shows that various optical schemes with some similarities have been reported. These include optical coherence tomography[47–49] and dispersion-free delay lines for measurements of ultrashort laser pulses[50, 51]. Here, we focused on Fourier transform spectrometry and its specific characteristics.

Based on the theoretical foundations, an optical scheme for an all-mirror infrared (IR) Fourier transform spectrometer has been proposed. The system offers several advantages over conventional systems, such as ultra-broad achromaticity and dispersion-free operation. The spectrometer features an increased throughput and scan length and the capability to dynamically adjust the split ratio between the interferometric arms. The system’s capabilities and performances have been demonstrated for various routine spectroscopic measurements; the high quality of absorption and dispersion spectra has been showcased. The operation of the system has been demonstrated by transmittance measurements of methane and polypropylene and by reflectance measurements of dried insulin products.

In the experimental part, a mid-IR supercontinuum source was used for pilot validation and as a proof-of-concept. The employed source has a limited spectral coverage (1.1 μm - 4.4 μm). However, we envisage great system capabilities for supercontinuum sources with much wider spectral coverage[24, 52–54], as well as for a range of other broadband laser systems including (but not limited to) Fabry–Pérot quantum cascade lasers or nonlinear systems—e.g., those based on standard parametric architectures or remarkable novel intrapulse difference frequency generation schemes[25, 55]. Such high spatial coherence broadband sources could utilize the full capabilities of the proposed interferometric system. In view of the ultra-broadband spectral response of the detector used, combined with the overall achromaticity of the system, the spectroscopic measurements, therefore, can be

performed over extremely wide spectral ranges. This is of great interest in, for instance, mid-IR spectroscopy and microscopy.

The careful reader may notice the possibility of miniaturization and simplification of the proposed spectrometer architecture. The wavefront dividing and combining prisms and the interferometer mirrors (M1 with M3 and M2 with M4) can be united into a metal-coated cube and two retroreflectors, respectively. This kind of modified system represents a compact solution with a 4-fold enhancement in the scan length. In addition, the use of pre-manufactured retroreflectors and cubes guarantees the stability of the optical scheme. Therefore, the use of similar modifications is anticipated in future due to their relevance for industrial and laboratory applications. This will support and stimulate further development of wavefront division Fourier transform spectroscopy techniques.

ACKNOWLEDGMENTS

Ivan Zorin is grateful to Andrii Prylepa for early discussions over a cup of coffee about the possibility of transferring the concept of wavefront division from OCT to spectrometry.

The authors would like to thank David Wimberger for preparing the insulin samples.

The authors acknowledge financial support from the European Union’s Horizon Europe Research And Innovation Programme Under Grant Agreement No.101057844 (Enviromed project).

This project is co-financed by research subsidies granted by the government of Upper Austria: Grant Nr. FTI 2022 (HIQUAMP): Wi-2021-303205/13-Au.

DATA AVAILABILITY STATEMENT

The data that support the findings of this study are available from the corresponding author upon reasonable request.

- [1] P. Griffiths, J. De Haseth, and J. Winefordner, *Fourier Transform Infrared Spectrometry*, Chemical Analysis: A Series of Monographs on Analytical Chemistry and Its Applications (Wiley, 2007).
- [2] J. M. Chalmers and P. R. Griffiths, eds., *Handbook of Vibrational Spectroscopy* (John Wiley & Sons, Ltd, Chichester, UK, 2002).
- [3] V. Saptari, *Fourier-Transform Spectroscopy Instrumentation Engineering* (SPIE, 2003) p. 136.
- [4] A. Dutta, in *Spectroscopic Methods for Nanomaterials Characterization*, Micro and Nano Technologies, edited by S. Thomas, R. Thomas, A. K. Zachariah, and R. K. Mishra (Elsevier, 2017) pp. 73–93.
- [5] A. Fathy, Y. M. Sabry, I. W. Hunter, D. Khalil, and T. Bourouina, *Laser & Photonics Reviews* **16**, 2100556 (2022).
- [6] S. Veerasingam, M. Ranjani, R. Venkatachalapathy, A. Bagaev, V. Mukhanov, D. Litvinyuk, M. Mugilarasan, K. Gurumoorthi, L. Guganathan, V. M. Aboobacker, and P. Vethamony, *Critical Reviews in Environmental Science and Technology* **51**, 2681 (2021).
- [7] S. Magalhães, B. J. Goodfellow, and A. Nunes, *Applied Spectroscopy Reviews* **56**, 869 (2021).
- [8] C. de Carvalho Almança Lopes, P. H. J. O. Limirio, V. R. Novais, and P. Dechichi, *Applied Spectroscopy Reviews* **53**, 747 (2018).
- [9] Z. Movasaghi, S. Rehman, and I. ur Rehman, *Applied Spectroscopy Reviews* **43**, 134 (2008).
- [10] H. Sreedhar, V. K. Varma, P. L. Nguyen, B. Davidson, S. Akkina, G. Guzman, S. Setty, A. Kajdacsy-Balla, and M. J. Walsh, *JoVE (Journal of Visualized Experiments)*, e52332 (2015).
- [11] R. Valand, S. Tanna, G. Lawson, and L. Bengtström, *Food Additives & Contaminants: Part A* **37**, 19 (2020), pMID: 31613710.
- [12] Y. Song, Y. Cong, B. Wang, and N. Zhang, *Expert Opinion on Drug Delivery* **17**, 551 (2020), pMID: 32116058.
- [13] A. A. Bunaciu, H. Y. Aboul-Enein, and S. Fleschin, *Applied Spectroscopy Reviews* **45**, 206 (2010).
- [14] F. Pavli, A. Argyri, G.-J. Nychas, C. Tassou, and N. Chorianopoulos, *Food Research International* **106**, 1061 (2018).
- [15] M. Erfan, Y. M. Sabry, M. Sakr, B. Mortada, M. Medhat, and D. Khalil, *Applied Spectroscopy* **70**, 897 (2016), pMID: 27044847.
- [16] A. Fathy, Y. M. Sabry, S. Nazeer, T. Bourouina, and D. A. Khalil, *Microsystems & Nanoengineering* **6**, 10 (2020).
- [17] J. Cohen, “Introduction to fourier transform spectroscopy;,” (1986).
- [18] R. S. Jackson, “Continuous scanning interferometers for mid-infrared spectrometry,” in *Handbook of Vibrational Spectroscopy* (John Wiley & Sons, Ltd, 2006) Chap. 1, pp. 1–19.
- [19] L. H. Kidder, A. S. Haka, and E. N. Lewis, “Instrumentation for ft-ir imaging,” in *Handbook of Vibrational Spectroscopy* (John Wiley & Sons, Ltd, 2006) Chap. 2, pp. 1–19.
- [20] D. A. Van Baak, *The Physics Teacher* **33**, 497 (1995).
- [21] P. Shukla, J. Lawrence, and Y. Zhang, *Optics & Laser Technology* **75**, 40 (2015).
- [22] G. Genty, A. T. Friberg, and J. Turunen, in *Progress in Optics*, Vol. 61, edited by T. D. Visser (Elsevier, 2016) pp. 71–112.
- [23] I. Zorin, P. Gattinger, A. Ebner, and M. Brandstetter, *Opt. Express* **30**, 5222 (2022).
- [24] R. A. Martinez, G. Plant, K. Guo, B. Janiszewski, M. J. Freeman, R. L. Maynard, M. N. Islam, F. L. Terry, O. Alvarez, F. Chenard, R. Bedford, R. Gibson, and A. I. Ifarraguerri, *Opt. Lett.* **43**, 296 (2018).
- [25] R. Krebbers, K. van Kempen, F. J. M. Harren, S. Vasilyev, I. F. Peterse, S. Lückner, A. Khodabakhsh, and S. M. Cristescu, *Opt. Express* **32**, 14506 (2024).
- [26] I. Zorin, J. Kilgus, K. Duswald, B. Lendl, B. Heise, and M. Brandstetter, *Applied Spectroscopy* **74**, 485 (2020), pMID: 32096412.
- [27] K. E. Jahromi, M. Nematollahi, R. Krebbers, M. A. Abbas, A. Khodabakhsh, and F. J. M. Harren, *Opt. Express* **29**, 12381 (2021).
- [28] M. A. Abbas, K. E. Jahromi, M. Nematollahi, R. Krebbers, N. Liu, G. Woyessa, O. Bang, L. Huot, F. J. M. Harren, and A. Khodabakhsh, *Opt. Express* **29**, 22315 (2021).
- [29] R. Krebbers, N. Liu, K. E. Jahromi, M. Nematollahi, O. Bang, G. Woyessa, C. R. Petersen, G. Van Rooij, F. J. M. Harren, A. Khodabakhsh, and S. M. Cristescu, *Scientific Reports* **12**, 9642 (2022).
- [30] L. Mandel, *Opt. Lett.* **16**, 1882 (1991).
- [31] G. Vdovin, F. van Goor, Guyskk, and L. Doyle, “Lightpipes - simulations of optical phenomena where diffraction is essential,” <https://github.com/opticspy/lightpipes> (2024).
- [32] M. Born, E. Wolf, A. B. Bhatia, P. C. Clemmow, D. Gabor, A. R. Stokes, A. M. Taylor, P. A. Wayman, and W. L. Wilcock, *Principles of Optics: Electromagnetic Theory of Propagation, Interference and Diffraction of Light*, 7th ed. (Cambridge University Press, 1999).
- [33] R. N. Bracewell, *The Fourier transform and its applications*, 3rd ed., McGraw-Hill series in electrical and computer engineering (McGraw Hill, Boston, 2000).
- [34] F. W. King, *Hilbert Transforms*, Encyclopedia of Mathematics and its Applications (Cambridge University Press, 2009).
- [35] A. W. Lohmann, D. Mendlovic, and Z. Zalevsky, *Opt. Lett.* **21**, 281 (1996).
- [36] J. R. Wubs, U. Macherius, X. Lü, L. Schrottke, M. Budden, J. Kunsch, K.-D. Weltmann, and J.-P. H. van Helden, *Applied Sciences* **14** (2024), 10.3390/app14103967.
- [37] A. Dabrowska, S. Lindner, A. Schwaighofer, and B. Lendl, *Spectrochimica Acta Part A: Molecular and Biomolecular Spectroscopy* **286**, 122014 (2023).
- [38] T. G. Mayerhöfer, A. Dabrowska, A. Schwaighofer, B. Lendl, and J. Popp, *ChemPhysChem* **21**, 707 (2020).
- [39] D. R. J. Boyd, H. W. Thompson, and R. L. Williams, *Proceedings of the Royal Society of London. Series A. Mathematical and Physical Sciences* **213**, 42 (1952).
- [40] I. Gordon, L. Rothman, R. Hargreaves, R. Hashemi, E. Karlovets, F. Skinner, E. Conway, C. Hill, R. Kochanov, Y. Tan, P. Wcislo, A. Finenko, K. Nelson, P. Bernath, M. Birk, V. Boudin, A. Campargue, K. Chance, A. Coustenis, B. Drouin, J. Flaud,

- R. Gamache, J. Hodges, D. Jacquemart, E. Mlawer, A. Nikitin, V. Perevalov, M. Rotger, J. Tennyson, G. Toon, H. Tran, V. Tyuterev, E. Adkins, A. Baker, A. Barbe, E. Canè, A. Császár, A. Dudaryonok, O. Egorov, A. Fleisher, H. Fleurbaey, A. Foltynowicz, T. Furtenbacher, J. Harrison, J. Hartmann, V. Horne- man, X. Huang, T. Karman, J. Karns, S. Kassi, I. Kleiner, V. Kofman, F. Kwabia-Tchana, N. Lavren- tieva, T. Lee, D. Long, A. Lukashetskaya, O. Lyulin, V. Makhnev, W. Matt, S. Massie, M. Melosso, S. Mikhailenko, D. Mondelain, H. Müller, O. Nau- menko, A. Perrin, O. Polyansky, E. Raddaoui, P. Ras- ton, Z. Reed, M. Rey, C. Richard, R. Tóbiás, I. Sadiek, D. Schwenke, E. Starikova, K. Sung, F. Tamassia, S. Tashkun, J. Vander Auwera, I. Vasilenko, A. Viganin, G. Villanueva, B. Vispoel, G. Wagner, A. Yachmenev, and S. Yurchenko, *Journal of Quantitative Spectroscopy and Radiative Transfer* **277**, 107949 (2022).
- [41] J. R. Birch, *Microchimica Acta* **93**, 105 (1987).
- [42] T. J. Parker, *Contemporary Physics* **31**, 335 (1990).
- [43] E. E. Bell, “Optical constants and their measurement,” in *Light and Matter Ia / Licht und Materie Ia*, edited by L. Genzel (Springer Berlin Heidelberg, Berlin, Heidel- berg, 1967) pp. 1–58.
- [44] J. Karger-Kocsis, ed., “Infrared and raman spectroscopy of polypropylene,” in *Polypropylene: An A-Z reference* (Springer Netherlands, Dordrecht, 1999) pp. 320–328.
- [45] J. Kilgus, G. Langer, K. Duswald, R. Zimmerleiter, I. Zorin, T. Berer, and M. Brandstetter, *Opt. Express* **26**, 30644 (2018).
- [46] S. Delbeck and H. M. Heise, *Journal of Diabetes Science and Technology* **15**, 865 (2021), PMID: 32281880.
- [47] A. G. Podoleanu, *Opt. Express* **15**, 9867 (2007).
- [48] N. Zhang, Q. Miao, C. C. Li, and P. Xue, *Optics Com- munications* **285**, 1589 (2012).
- [49] J. Yin, Q. Miao, and P. Xue, in *Fifth International Conference on Photonics and Imaging in Biology and Medicine*, Vol. 6534, edited by Q. Luo, L. V. Wang, V. V. Tuchin, and M. Gu, International Society for Optics and Photonics (SPIE, 2007) p. 653406.
- [50] H. Mashiko, A. Suda, and K. Midorikawa, *Applied Physics B* **76**, 525 (2003).
- [51] A. Tyagi, M. S. Sidhu, A. Mandal, S. Kapoor, S. Dahiya, J. M. Rost, T. Pfeifer, and K. P. Singh, *Scientific Reports* **12**, 8525 (2022).
- [52] C. R. Petersen, U. Møller, I. Kubat, B. Zhou, S. Dupont, J. Ramsay, T. Benson, S. Sujecki, N. Abdel-Moneim, Z. Tang, D. Furniss, A. Seddon, and O. Bang, *Nat. Pho- tonics* **8**, 830 (2014).
- [53] Z. Zhao, B. Wu, X. Wang, Z. Pan, Z. Liu, P. Zhang, X. Shen, Q. Nie, S. Dai, and R. Wang, *Laser Photonics Rev* **11**, 1700005 (2017).
- [54] M. Zhang, L. Li, T. Li, F. Wang, K. Tian, H. Tao, X. Feng, A. Yang, and Z. Yang, *Opt. Express* **27**, 29287 (2019).
- [55] U. Elu, L. Maidment, L. Vamos, F. Tani, D. Novoa, M. H. Frosz, V. Badikov, D. Badikov, V. Petrov, P. St. J. Rus- sell, and J. Biegert, *Nature Photonics* **15**, 277 (2021).